Research Article Vol. 33, No. 23 / 17 Nov 2025 / Optics Express 48140

Optics EXPRESS

Ultrafast laser damage: the effect of an adhesion layer on damage thresholds

CHRISTOPH B. MORSCHER[1,2,*] **AND PAUL PLANKEN**[1,2]

[1] *Advanced Research Center for Nanolithography (ARCNL), Science Park 106, 1098 XG Amsterdam, The Netherlands*
[2] *Van der Waals-Zeeman Institute, Institute of Physics, University of Amsterdam, Science Park 904, 1098 XH Amsterdam, The Netherlands*
[*] *c.morscher@arcnl.nl*

Abstract: Sub-picsosecond laser-induced damage (LID) is intrinsically linked to material properties. Due to the weak adhesion of gold on dielectric substrates, LID is visible as delamination at very low fluence thresholds. Adding a chromium adhesion layer between the gold and the substrate increases damage thresholds for single laser shots by a factor of three. Surprisingly, for multishot experiments, little or no increase in the optical damage threshold is observed.

1. Introduction

Ultra-short pulsed lasers are increasingly utilized in numerous industrial applications, ranging from 2-photon microscopy in medicine and biology [1,2] to material processing and optical metrology in semi-conductor device manufacturing and metal/steel processing [3–6]. However, due to the requirement of high optical powers, the risk of laser-induced damage on optical elements, for example a mirror, increases significantly. Thus, engineering of the materials from the perspective of laser damage becomes increasingly important. Gold is a common material used for NIR and Deep IR mirrors [7] and at the same time, it has been extensively studied in the field of ultra-short laser physics as a model material [8–10]. From preceding studies on material science, it is known that thin films of gold do not adhere well to dielectric substrates like fused silica [11–13]. As a result, illumination with high fluence laser pulses can lead to delamination and subsequent tearing of the thin film from the substrate [14–16]. In order to improve the attachment of the gold film onto the fused silica, a chromium adhesion layer is commonly used [11–13]. In principle, this should increase the laser damage thresholds, as delamination is more or less prevented. Using an amplified femto-second laser, we have performed optical damage experiments on two types of samples: a 50 nm gold thin film on fused silica with, and without a 5 nm chromium adhesion layer. We demonstrate that for single pulse illumination, the ablation threshold for samples with an adhesion layer increases significantly. Surprisingly, we find that this is not the case for multi-pulse illumination. There, other damage mechanisms appear at fluence levels compared to those where for gold without adhesion layer, ablation/delamination is observed.

2. Experimental setup and working procedure

The first step in the sample preparation is the removal of organic residues and dust from the fused silica substrate (12 x 12 mm, 0.5 mm thick) using a standard base piranha solution. The thin films are deposited onto the cleaned substrate using E-beam deposition (Polyteknik Flextura M508 E). All gold thin films are 50 nm thick, while the chromium adhesion layer has a thickness of 5 nm.

Figure 1(a) shows a schematic drawing of the experimental setup. The laser pulses for the damage experiments are generated by an amplified Ti:Sapphire femtosecond laser (Femtopower HE3 from Femtolasers) at a repetition rate of 1 kHz, and have a pulse duration of 45 fs. After

#576574 https://doi.org/10.1364/OE.576574
Journal © 2025 Received 20 Aug 2025; revised 24 Oct 2025; accepted 26 Oct 2025; published 5 Nov 2025

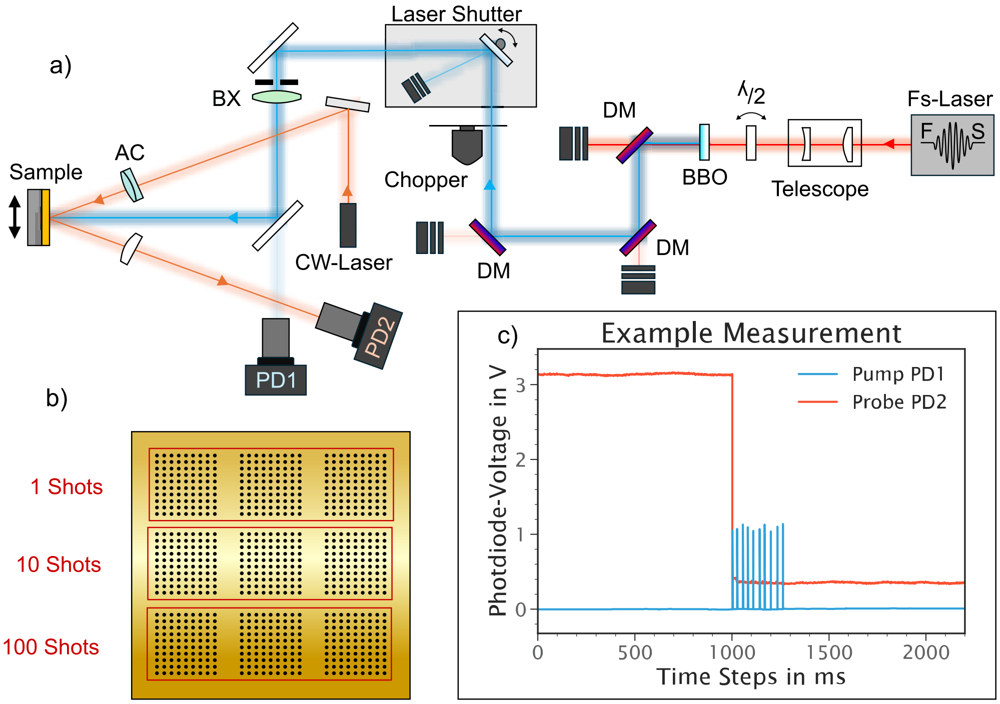

Fig. 1. (a) Schematic depiction of the experimental setup. A 45 fs laser pulse from an amplified Ti:sapphire laser is frequency doubled in a BBO crystal to a wavelength of 400 nm (blue beam). A pulse picker, consisting of a chopper and galvo-laser shutter, select a number of pulses, which are subsequently focused onto the sample. A CW laser measures the pump induced changes in the reflectivity of the sample. PD1 and PD2 are photodiodes. $\lambda/2$ is a half wave plate to rotate the laser beam, allowing intensity tuning of the second harmonic generation. DM are the dichroic mirrors that filter out the remaining fundamental laser beam. BX: biconvex lens. AC: Achromat lens. (b) Layout of the illumination pattern on the sample. Each black spot corresponds to a single 1, 10 and 100 shots exposure, where within each 10 x 10 grid, the fluence varies in a scanning fashion from left to right. (c) Example measurement at one exposure site. the reference photodiode of the pump records the number of pulses released and their respective fluences, while the probe photodiode PD2 measures the change of reflection continuously, starting one second before the pump illuminates the sample and stopping 1 second after pump illumination.

passing through the telescope that reduces the beam diameter from 3 mm to 1 mm, the laser beam propagates through a half-wave plate and a BBO crystal, for second harmonic generation at 400 nm wavelength. Using the motorized rotation of the half-wave plate, the output power of the second harmonic beam can be changed, allowing different fluences for the exposure at the sample. A sequence of three dichroic mirrors filters out the remaining fundamental beam, while transmitting the second harmonic beam. An optical chopper (Thorlabs MC2000B-EC), that reduces the repetition rate to 100 Hz, and the galvo-mirror based ultrafast laser shutter (Optogama) select the desired number of pulses that hit the target. An aperture in front of the focusing biconvex lens (Thorlabs LB4453, f = 500 mm) clips the beam to create a cleaner spatial profile (140 µm FWHM) at the sample at the cost of about 30 % power loss. A silicon amplified photodiode (Thorlabs PDA 100 A2) is placed behind the last mirror, which measures pump light leakage through the mirror of each pulse during the experiments.

During the exposure experiments, a continuous wave laser (Thorlabs PL202, 0.9 mW, 635 nm) is used to continuously measure the reflectivity of the sample surface. It is focused under an angle of about 10 degrees with respect to the pump laser at the center of the pump laser spot using an achromatic lens (Thorlabs AC254-100-A, f = 100 mm, spot diameter 56 µm FWHM). The reflected light is collected by a lens with the same focal length (Thorlabs LA1509-A, f = 100 mm) and is finally measured by a amplified silicon photodiode (Thorlabs PDA 100 A2).

The sample surface is divided into a total of nine separate measurement areas, each contains 100 exposure sites (represented in Fig. 1(b) as a black dot). For each 10x10 area, the number of pulses is kept constant and instead, the fluence per pulse is gradually changed from exposure site to exposure site. Three measurement areas (indicated by the red rectangles in Fig. 1(b)) are assigned to experiments, with 1, 10 and 100 shots per exposure site respectively. At each exposure site, the laser shutter opens and transmits the specified number of pulses with a specified fluence, which the pump reference photodiode measures as a voltage signal for each pulse. Meanwhile, the probe photodiode continuously measures the reflection off the sample, starting 1000 ms before the pump pulse illuminates the sample and stopping after 1000 ms post-illumination. Lastly, the sample stage moves 250 μm to the next exposure site for the next measurement and stops after all 100 sites have been illuminated. Due to the limited available space on the samples, exposures were restricted to a maximum of 100 laser shots.

The pre-processing of the acquired data is done as follows (details in Supplement 1): the relative reflection change ΔR is obtained by taking the average of the 1000 probe reflection values before pump illumination $\overline{R}_{pre}$ and 1000 reflection values after the pump illumination $\overline{R}_{post}$, calculating ΔR:

$$\Delta R = \frac{\overline{R}_{post} - \overline{R}_{pre}}{\overline{R}_{pre}}. \tag{1}$$

The conversion of the pump photodiodes voltage to the respective fluence for each pulse is done by measuring the beam profile and performing a power to photo-diode-voltage calibration, with the power meter placed at the sample's location (details can be found in Supplement 1 section).

Characterization of damaged sites is done by optical microscopy (OM) in dark-field and bright-field mode (Zeiss Axioskop2 MAT) and by Scanning Electron Microscopy (FEI Verios 460). The determination of all damage thresholds is performed on optical microscope images using the Liu method [17] by calculating the area of the damage sites by ellipse fitting or by counting the number of pixels, where damage is observed. Plotting the retrieved area against the natural logarithm of the fluence yields a linear relationship, where the fluence thresholds are found by the intersection of the linear fitted line with the x-axis (see Supplement 1 section for more details).

3. Results

Figure 2 displays the scatter plot for all datasets on the sample without an adhesion layer (reference sample). The relative reflection change of the sample surface is plotted against the average fluence per pulse. For all experiments, a slight positive increase of the relative reflection change is seen at a fluence at around 12 mJ/cm^2, which could be an indication of delamination as observed in previous studies [14,15]. Further increasing the fluence shows that after a certain threshold, the reflection changes sharply by 80 %. For 100 shots, this drop appears at lower fluences (16 mJ/cm^2) than for the 10 shots (19 - 21 mJ/cm^2) and for the one shot (25 mJ/cm^2) exposures. Lastly, the scatter plot for single pulse exposures reveals a cluster of data points that exhibit a comparatively lower relative change in reflection at the corresponding fluences.

Optical bright field images of the sites exposed to a fluence where this steep reflection change occurs, are depicted in Fig. 3(I) and (II), and are marked with the same label in the scatter plot

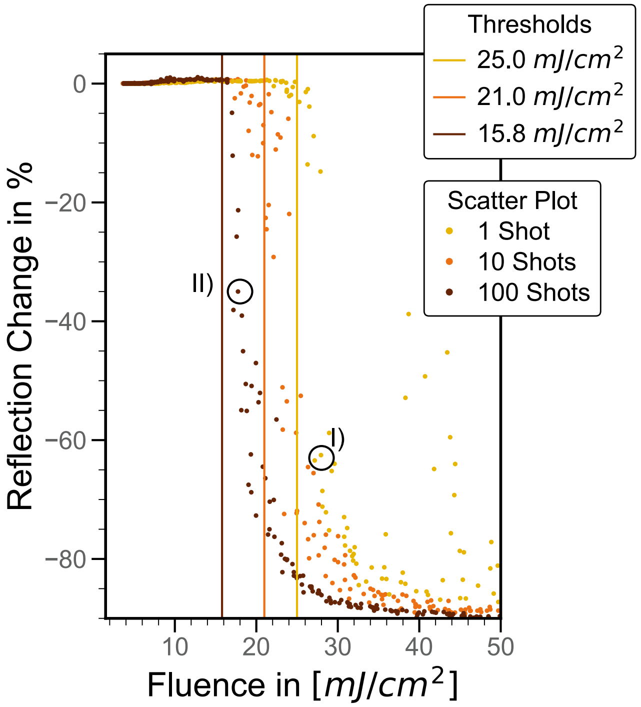

Fig. 2. Scatter plots of the relative reflection changes versus fluence per pulse for 1 laser shot (yellow dots), 10 shots (orange dots) and 100 shots (brown dots) for a 50 nm gold on fused silica without adhesion layer. The vertical lines indicate the ablation thresholds for the respective number of shots (yellow: 1 Shot, orange: 10 Shots, brown: 100 Shots).

of Fig. 2. It can be seen that the black hole, corresponding with ablation, here defined as the significant removal of material, correlates with the steep drop in reflection. Furthermore, for both cases, the 1 shot (Fig. 3, I) and the 100 shots craters Fig. 3, II) show ruptures and cracks reminiscent of torn paper, which has been observed also in previous studies for single pulse illumination [14,15]. Using the optical microscope images of all illuminated sites, the ablation thresholds are determined and plotted in Fig. 2 as straight vertical lines. A comparison of the lines shows the same trend as observed in the sharp reflection decrease: The higher the number of shots, the lower the ablation threshold.

Figure 4 depicts the relative reflection change of the sample surface plotted against the average fluence per pulse for all three numbers of shots on the sample with the adhesion layer. All scatter plots show the same steep reflection decrease due to ablation. However, they occur at significantly higher fluence ranges (74 to 84 mJ/cm^2 compared to 16 - 25 mJ/cm^2) for the sample without an adhesion layer. While the single shot measurements do not display significant reflection changes before ablation, both the 10 shots and 100 shots do: the 10 shots measurement displays a gentle drop before ablation (starting at a fluence of around 50 mJ/cm^2), and the 100 shots measurement show a more gradual drop starting at around 23 mJ/cm^2, followed by an increase of relative reflectivity starting at around 40 mJ/cm^2). Lastly, a small dip in the reflectivity is visible at around 15 mJ/cm^2. These changes are indicative of another form of damage other than ablation, which is only observed for multi-shot measurements. Figure 3 shows bright-field images of the ablation craters from the sample with a 5 nm chromium adhesion layer (Fig. 3, III and IV). It can be seen that the ablation craters look very different in comparison to the sample without an

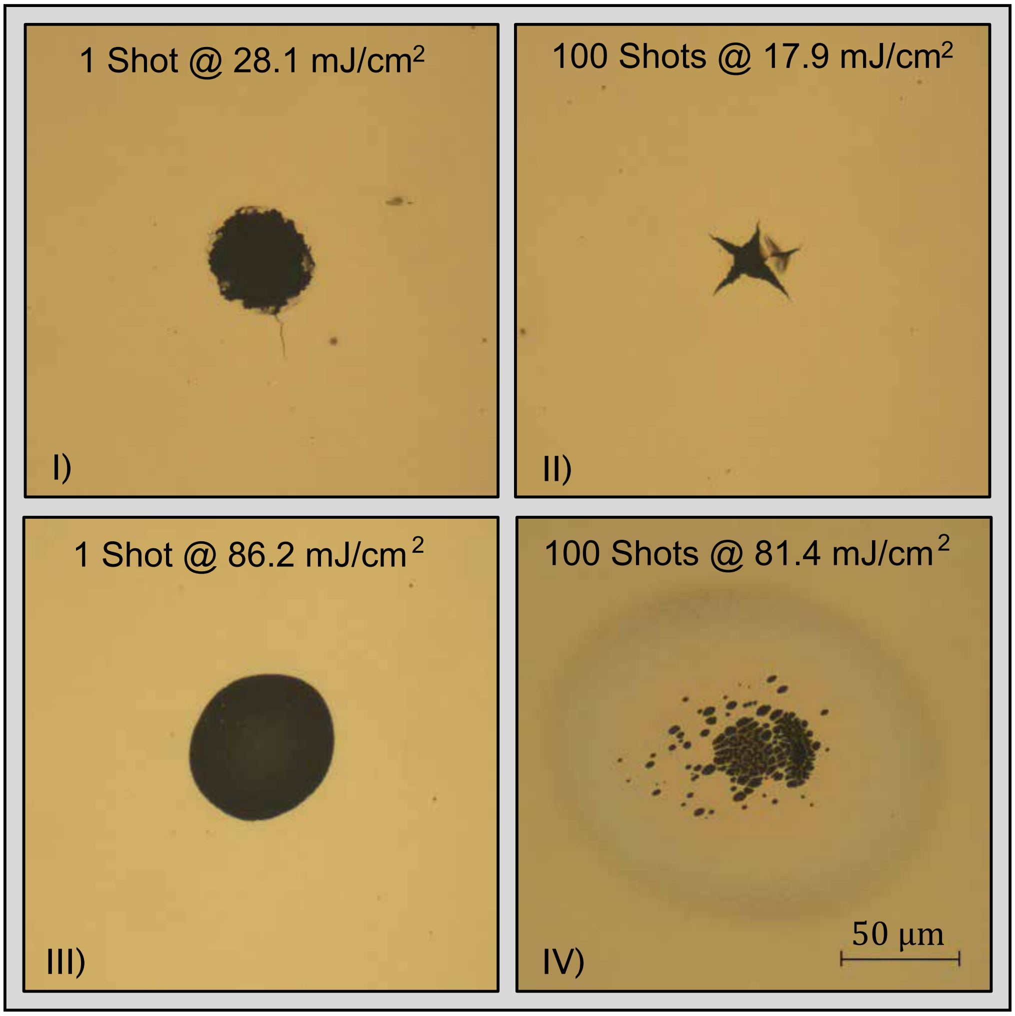

Fig. 3. Brightfield microscopy images showing typical ablation craters for the gold thin film sample without adhesion layer (I : 1 shot, II : 100 shots) and for the sample with an adhesion layer (III : 1 shot, IV: 100 shots). The respective fluence per pulse is shown in the image as well. Image I) and II) are also marked in the scatter plots of Fig. 2. The scale bar applies to all images.

adhesion layer (Fig. 3 I and II). The rupturing is not observed anymore and instead the craters edges are smooth for the 1 shot illumination sites while the 100 shots illumination sites show an agglomeration of small holes. Furthermore, a ring with discoloration is visible around the agglomeration. These observations so far indicate a strong impact of the adhesion layer on the optical damage.

To further investigate each visible trend for the 100 shots, dark-field images of each data point, marked in Fig. 4, are displayed in Fig. 5. The image with label V, shows a bright diffusive spot at an exposure fluence of 25.7 mJ/cm^2 that eventually transitions to quasi-periodic structures, visible in image 5.VI for an exposure fluence of 43.1 mJ/cm^2. Increasing the fluence further shows that the surface appears smooth again (Image VII, at exposure fluences of 75.3 mJ/cm^2) before ablation features, such as small hole agglomeration, begin to appear (5.VIII, at exposure

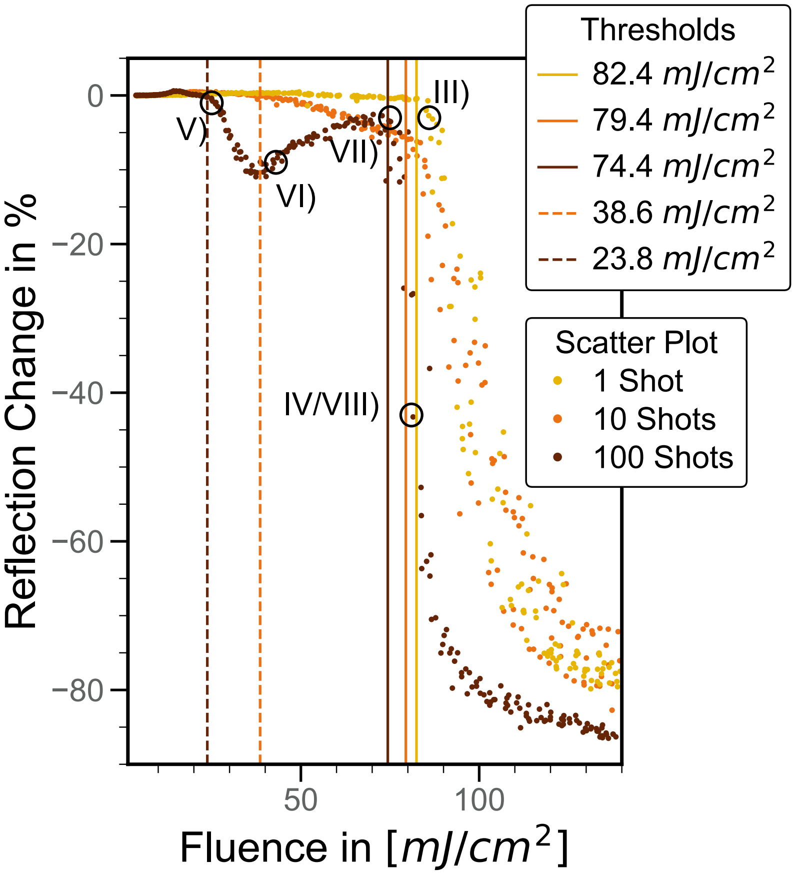

Fig. 4. Scatter plots of the relative reflection changes versus average fluence per pulse for 1 laser shot (yellow dots), 10 shots (orange dots) and 100 shots (brown dots) for 50 nm gold with a 5 nm chromium adhesion layer on fused silica. The vertical lines indicate the ablation (straight lines) and damage thresholds (dashed lines) for the respective number of pulses.

fluences of 81.4 mJ/cm^2). The last image (VIII) shows the same illuminated area as the image in Fig. 3 IV and it is clear that the rough and semi-periodic structures are linked to the observed discoloration. These observations also match with the respective measured reflection changes where the roughening and semi-periodic structures lead to less specular reflected light, while the smooth surface before ablation is associated with an increase of reflected light. Like before, the ablation thresholds are displayed as solid lines in Fig. 4 for each respective number of pulses. Furthermore, a general damage threshold can be determined from, the dark-field images based on the earliest sign of visual change, other than ablation. These thresholds are plotted as dashed lines in Fig. 4. While ablation thresholds appear to be significantly larger compared to the reference sample without an adhesion layer, this is not the case anymore when considering any surface modification in general. Then, the observed damage thresholds for multi-shot illumination are not much higher than the ones for the gold sample without adhesion layer.

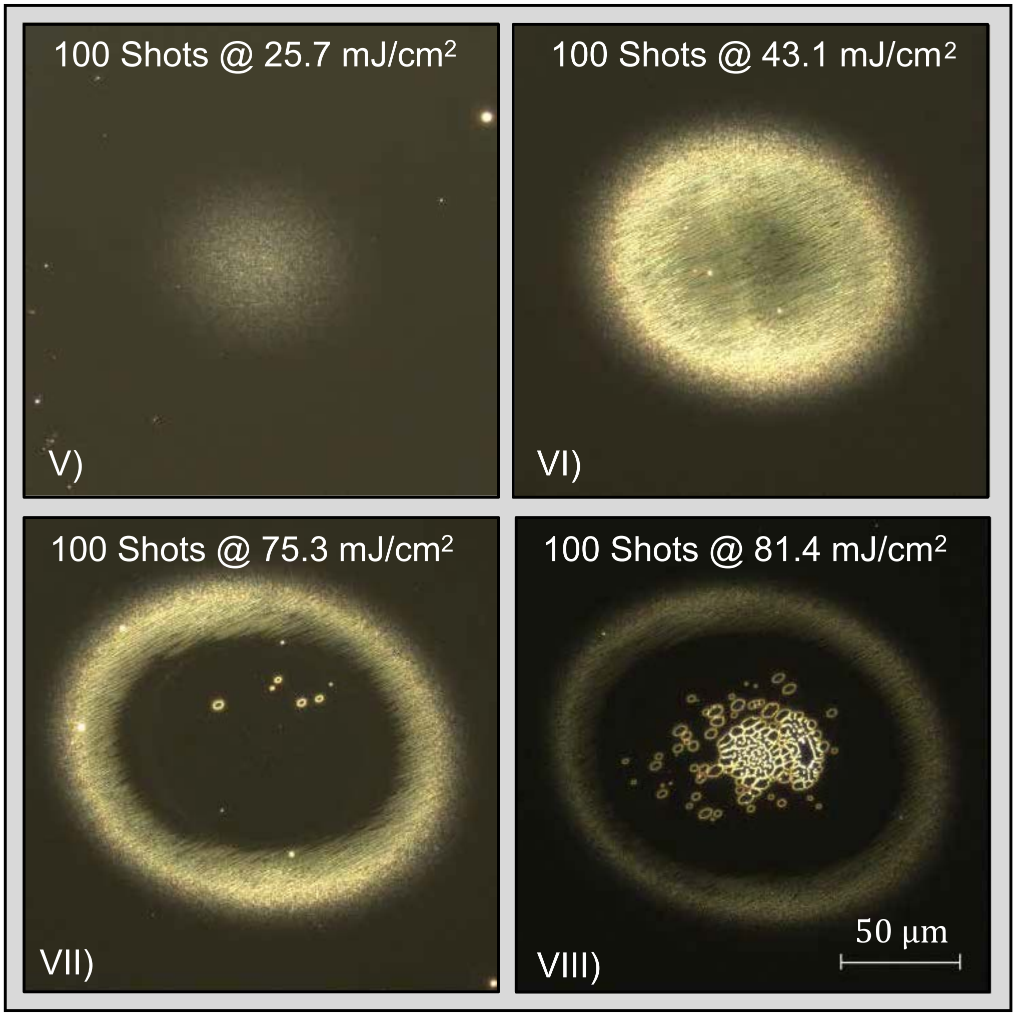

Fig. 5. Dark-field microscope images obtained after exposure of the adhesion layer sample containing 50 nm of gold and 5 nm of chromium to 100 laser shots at four different fluences, indicated in the figure.

4. Discussion

The observed damage and ablation mechanisms are very much dependent on the material properties of the sample. For the gold thin film sample without an adhesion layer, the primary observed laser damage mechanism is delamination, followed by rupturing due to the weak adhesion of the thin film to the substrate [14]. This mechanism is observed as cracks and tears at the respective ablation area for 1, 10 and 100 shots (Fig. 3 I and II). The sharp reflection drop corresponds to ablation, as less light is reflected from the sample surface due to the ablation crater. The determined thresholds, as well as the reflection drop, show that low fluences are sufficient to effectively remove material, which agrees with the weak attachment of the gold to the substrate. The observed cluster of data points showing a relatively lower change in reflection can be attributed to the fact that, during the delamination process, some flakes remain within the ablated area.

Introducing an adhesion layer increases the attachment of the gold thin film to the glass substrate [11–13], and hence effectively removes the weakness of poor adhesion. It would seem that this should increase the damage thresholds, as delamination is not the primary damage mechanism anymore. This observation is correct if only full ablation is considered, where the required fluence for effective material removal is about three times higher for all three tested numbers of pulses. It is also visible that the mechanism of ablation is not delamination anymore as the corresponding bright-field images do not show tears and cracks. Instead, the single shot image displays elliptical ablation craters with smooth edges as the only visual change under the microscope. These images correspond to the data points where the reflectivity sharply drops due to ablation. The ablation mechanism in this case appears to be most likely vaporization, as it looks similar to earlier results from ultrafast ablation measurements on thin films [18]. This hypothesis cannot be conclusively verified, as only the incident fluence was measured. To provide supporting evidence, it would be necessary to determine the total absorbed energy per unit volume, enabling a direct comparison with the vaporization energy required to remove the material within the crater.

The multi-shot experiments, however, already show changes in reflectivity before full ablation occurs. This indicates that ablation is not the only damage mechanism. Following the reflection curve representing the 100 shots measurements in Fig. 4, the first drop in reflectivity is linked to the observed increased scattering visible in the dark-field image (Fig. 5(V)). This is most likely due to roughening of the surface that eventually evolves into laser-induced periodic surface structures due to melting and resolidification (LIPSS, Fig. 5(VI)), which has been already extensively described in literature [19,20]. It should be noted that the semi-periodic surface modifications, observed in the microscope images in Fig. 5(VI), are not the LIPSS pattern itself. The periodicity of the LIPSS pattern typically corresponds to values around the laser wavelength [20], which cannot be resolved with a conventional microscope objective. Figure 6 shows a SEM Image taken from the same exposure side from Fig. 5(VI) at a higher magnification, where the LIPSS pattern are clearly visible.

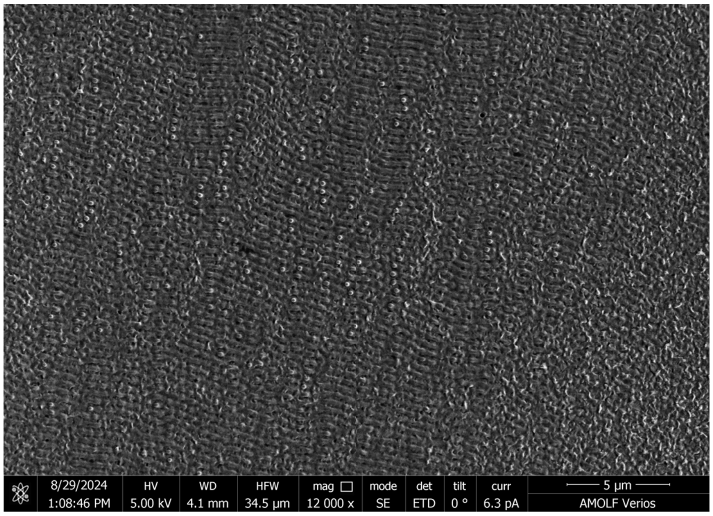

Fig. 6. Example image of the LIPSS Pattern, taken from the SEM of the exposure sites of the sample with the adhesion layer (illuminated by 100 shots at a peak fluence per pulse of 43.1 mJ/cm^2). This exposure site is the same as shown in Fig. 5VI.

The mechanism that causes the large structure which is observed in the dark-field images, is unclear at the moment. The transition to a smooth surface (Fig. 5(VII)), when the optical fluence is increased further, is currently under investigation. Possible hypotheses include the removal of the LIPSS pattern via gentle ablation and/or further melting and re-solidification of the material. Before the ablation crater formation, the agglomeration of holes was observed, which are reminiscent of dewetting, which has been observed in the past for gold thin films as well, although with a titanium adhesion layer [21]. The 10 shots experiment shows in principle the same behavior as the 100 shots one, except that the surface smoothing is not observed and instead, ablation/de-wetting appears to follow the LIPSS formation directly.

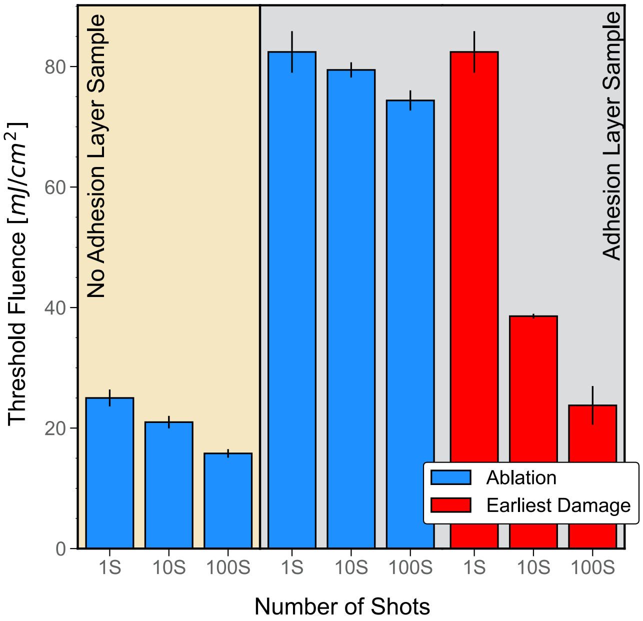

Fig. 7. Bar plot of all determined optical damage thresholds for the sample with (gray background) and without (yellow background) an adhesion layer. Blue bars indicate the *ablation* thresholds, red bars indicate earliest visible damage thresholds. The 1 shot experiment on the adhesion layer has ablation as its first visible damage and therefore its red and blue bars are the same. The error bars were the retrieved from statistical fitting procedure during threshold determination (see Supplement 1).

For the 1, 10 and 100 shots experiments on the sample without the adhesion layer, the first observed change under the optical microscope is ablation. This is also the case for the 1 shot experiment on the sample with the adhesion layer. For the 10 and the 100 shots experiments on the same sample, earlier signs of damage are observed before ablation starts. Therefore, a separate threshold is determined for that form of damage. All thresholds, which are depicted as vertical lines in Fig. 2 and Fig. 4 are combined in a bar plot, depicted in Fig. 7 together with their respective error margins. These are obtained from the statistical fitting procedure during the threshold determination (see Supplement 1). When comparing only ablation thresholds (Fig. 7, blue bars), it appears that the optical damage threshold increases by about 3 times by adding an adhesion layer. However, when considering all visible surface modification induced by the laser, more specifically the first observed roughening and subsequent LIPSS formation, then the difference between the thresholds between both samples is smaller. For the 100 shots case, the difference amounts to only about 60 % (15.8 mJ/cm^2 no adhesion layer vs 23.8 mJ/cm^2 with adhesion layer). Since all thresholds are determined using optical microscopy, the accuracy of the determined threshold values are limited by this inspection technique. More subtle changes, potentially visible under SEM or AFM could result in lower thresholds. Furthermore, during the threshold determination, two approaches were employed to determine the damaged area: for elliptical/circular craters, like the 1 shot experiment on the sample with an adhesion layer, ellipse fitting to the images was used, following Liu's method. For non-elliptical crater images, like the ruptures of 100 shots on the sample without adhesion layer, a simple ablation pixel count was employed, due to the challenge of fitting an ellipse to a non-elliptical damaged spot (details in Supplement 1). To test both approaches, ellipse fitting and pixel counting have been employed for the 1 shot experiment on the adhesion layer sample for comparison (see Supplement 1). It appears that the impact of the method for damage area determination on the threshold value is fairly small, with a difference of less than 0.3 mJ/cm^2, which is within the error margin of our threshold determination.

5. Conclusion

In summary, we studied the impact of adding an adhesion layer between gold thin film and a fused silica substrate on laser damage thresholds in single- and multi-pulse illumination experiments. For the sample without the adhesion layer, the delamination due to the weak adhesion appeared as expected for all experiments, leading to rather low damage thresholds [14]. The experiments on the sample with an adhesion layer, however showed interesting results: When considering only ablation as the damage mechanism, the damage thresholds compared to the reference sample increased by a factor of three, particularly in the case of single pulse illumination. For the multi-pulse illumination, however, other laser-induced damage mechanisms like LIPSS were observed at significantly lower fluences. When taking these different damage mechanisms into consideration, then the differences in thresholds between the gold layers with and without an adhesion layer was much smaller. Our results show that adding an chromium adhesion layer only has a limited effect on the optical damage threshold.

Acknowledgment. This work was conducted at the Advanced Research Center for Nanolithography, a public-private partnership between the University of Amsterdam, Vrije Universiteit Amsterdam, University of Groningen, the Netherlands Organization for Scientific Research (NWO), and the semiconductor equipment manufacturer ASML. The authors thank Thomas Meijvogel, Igor Hoogsteder, Dylan Loozen and Bob Drent for technical support.

Disclosures. The authors declare no conflicts of interest.

Data availability. Data underlying the results presented in this paper may be obtained from the authors upon reasonable request.

Supplemental document. See Supplement 1 for supporting content.

References

1. C. L. Hoy, O. Ferhanoğlu, M. Yildirim, *et al.*, "Clinical Ultrafast Laser Surgery: Recent Advances and Future Directions," IEEE J. Sel. Top. Quantum Electron. **20**(2), 242–255 (2014).
2. I. V. Ilina and D. S. Sitnikov, "Application of Ultrashort Lasers in Developmental Biology: A Review," Photonics **9**(12), 914 (2022).
3. M. Malinauskas, A. Žukauskas, S. Hasegawa, *et al.*, "Ultrafast laser processing of materials: From science to industry," Light: Science Applications **5**(8), e16133 (2016).
4. K. Sugioka, "Progress in ultrafast laser processing and future prospects," Nanophotonics **6**(2), 393–413 (2017).
5. N. G. Orji, M. Badaroglu, B. M. Barnes, *et al.*, "Metrology for the next generation of semiconductor devices," Nat. Electron. **1**(10), 532–547 (2018).
6. Y. Shimizu, L.-C. Chen, D. W. Kim, *et al.*, "An insight into optical metrology in manufacturing," Meas. Sci. Technol. **32**, 042003 (2021).
7. J. P. Gardner, J. C. Mather, M. Clampin, *et al.*, "The James Webb Space Telescope," Space Sci. Rev. **123**(4), 485–606 (2006).
8. B. J. Demaske, V. V. Zhakhovsky, N. A. Inogamov, *et al.*, "Ablation and spallation of gold films irradiated by ultrashort laser pulses," Phys. Rev. B **82**(6), 064113 (2010).
9. T. Pflug, J. Wang, M. Olbrich, *et al.*, "Case study on the dynamics of ultrafast laser heating and ablation of gold thin films by ultrafast pump-probe reflectometry and ellipsometry," Appl. Phys. A **124**(2), 116 (2018).
10. M. Segovia and X. Xu, "High Accuracy Ultrafast Spatiotemporal Pump–Probe Measurement of Electrical Thermal Transport in Thin Film Gold," Nano Lett. **21**(17), 7228 (2021).
11. M. Todeschini, A. Bastos da Silva Fanta, F. Jensen, *et al.*, "Influence of Ti and Cr Adhesion Layers on Ultrathin Au Films," ACS Applied Materials Interfaces **9**(42), 37374–37385 (2017).

12. D. M. Mattox, “Thin film metallization of oxides in microelectronics,” Thin Solid Films **18**(2), 173–186 (1973).
13. A. Munitz and Y. Komem, “Structural and resistivity changes in heat-treated chromium-gold films,” Thin Solid Films **37**(2), 171–179 (1976).
14. E. Abram, I. Milov, N. Orlov, *et al.*, “Pre-ablation regime light-induced optical changes in nanometer thick metal films,” Opt. Express **32**(3), 4564–4587 (2024).
15. H. Huang, L. Wang, F. Kong, *et al.*, “Effects of substrate on the femtosecond laser-induced damage properties of gold films,” Opt. Mater. **81**, 115–121 (2018).
16. J. Krüger, D. Dufft, R. Koter, *et al.*, “Femtosecond laser-induced damage of gold films,” Appl. Surf. Sci. **253**(19), 7815–7819 (2007).
17. J. M. Liu, “Simple technique for measurements of pulsed Gaussian-beam spot sizes,” Opt. Lett. **7**(5), 196–198 (1982).
18. M. Olbrich, E. Punzel, P. Lickschat, *et al.*, “Investigation on the Ablation of thin Metal Films with Femtosecond to Picosecond-pulsed Laser Radiation,” Phys. Procedia **83**, 93–103 (2016).
19. Y. Fuentes-Edfuf, J. A. Sánchez-Gil, C. Florian, *et al.*, “Surface Plasmon Polaritons on Rough Metal Surfaces: Role in the Formation of Laser-Induced Periodic Surface Structures,” ACS Omega **4**(4), 6939–6946 (2019).
20. A. Y. Vorobyev, V. S. Makin, and C. Guo, “Periodic ordering of random surface nanostructures induced by femtosecond laser pulses on metals,” J. Appl. Phys. **101**(3), 034903 (2007).
21. W. M. Abbott, C. P. Murray, C. Zhong, *et al.*, “Less is More: Improved Thermal Stability and Plasmonic Response in Au Films via the Use of SubNanometer Ti Adhesion Layers,” ACS Applied Materials Interfaces **11**(7), 7607–7614 (2019).